Rational design of Z-scheme PtS-ZnIn$_2$S$_4$/WO$_3$-MnO$_2$ for overall photocatalytic water splitting under visible light

Yao Ding[a], Dingqiong Wei[a], Rong He[a], Rusheng Yuan[a], Tengfeng Xie[b,*], Zhaohui Li[a,*]

[a] Research Institute of Photocatalysis, State Key Laboratory of Photocatalysis on Energy and Environment, College of Chemistry, Fuzhou University, Fuzhou 350116, PR China
[b] State Key Laboratory of Theoretical and Computational Chemistry, College of Chemistry, Jilin University, Changchun, Jilin, 130012, PR China

ARTICLE INFO

ABSTRACT

ZnIn$_2$S$_4$/WO$_3$ nanocomposites, with ZnIn$_2$S$_4$ nanosheets loaded on WO$_3$ nanorods, were synthesized by self-assembly of hexagonal ZnIn$_2$S$_4$ in the presence of preformed WO$_3$·H$_2$O nanoplates. PtS and MnO$_2$, the co-catalysts for H$_2$ and O$_2$ evolution, respectively, were selectively loaded on ZnIn$_2$S$_4$ and WO$_3$ in the nanocomposites. The resultant PtS-ZnIn$_2$S$_4$/WO$_3$-MnO$_2$ nanocomposites show photocatalytic activity for overall water splitting to produce H$_2$ and O$_2$ under visible light. An optimum activity was achieved over 0.5%PtS-20%ZnIn$_2$S$_4$/WO$_3$-3.0% MnO$_2$, in which 5.94 μmol of H$_2$ and 2.24 μmol O$_2$ were evolved in 8 h. The apparent quantum yield (AQY) for H$_2$ evolution was determined to be ca. 0.50% at 420 nm. The superior photocatalytic activity for overall water splitting over PtS-ZnIn$_2$S$_4$/WO$_3$-MnO$_2$ nanocomposites can be ascribed to an efficient coupling of photocatalytic water reduction over PtS-ZnIn$_2$S$_4$ and photocatalytic water oxidation over MnO$_2$-WO$_3$ via a Z-scheme charge transfer pathway. This study demonstrates a high potential of fabrication of the all-solid Z-scheme photocatalytic systems for overall water splitting.

1. Introduction

Since H$_2$ is an ideal clean fuel and a promising alternative to traditional fossil fuels, efficient conversion and storage of solar energy by photocatalytic water splitting to produce H$_2$ has been considered to be an ideal strategy to solve the current worldwide energy crisis and the serious environmental problems [1–4]. To achieve photocatalytic overall water splitting, water reduction to evolve H$_2$ and oxidation to evolve O$_2$ should occur simultaneously [5–10]. To realize this, the conduction band (CB) of the semiconductor-based photocatalyst should be more negative than E(H$^+$/H$_2$) (0 V vs NHE), while its valence band (VB) should be more positive than E(O$_2$/H$_2$O) (1.23 V vs NHE) [11]. In addition, a considerable over-potential for both H$_2$ and O$_2$ evolution is still required [12]. Usually it is difficult for a single-component photocatalyst to simultaneously possess wide light-absorption range and strong redox ability since these two conditions are mutually exclusive. As we know, an efficient utilization of solar light requires that the semiconductor should possess a narrow band gap, while more negative CB and more positive VB are thermodynamically beneficial for the redox reactions. Therefore, despite tremendous efforts has been devoted to develop visible light responsive photocatalysts, only a very limited single-component photocatalysts have been demonstrated to be active for overall water splitting under visible light [13].

A more efficient strategy for the development of photocatalysts for water splitting under visible light is to design Z-scheme photocatalytic systems which mimic that in the natural photosynthesis [14,15]. Different from the normal heterojunction-type charge transfer mechanism, the Z-scheme photocatalytic systems not only can features the spatial isolation of photogenerated electrons and holes, but also can retain the strong reducibility of photocatalyst I (PC I) and the strong oxidizability of photocatalyst II (PC II) (Scheme 1). The first generation of the artificial Z-scheme photocatalytic systems is comprised of two semiconductor photocatalysts and an electron acceptor/donor (A/D) pair as the electron mediator [16,17]. Frequently used electron mediators include IO$_3$$^-$/I$^-$, Fe^{3+}/Fe^{2+}, [Co(bpy)$_3$]$^{3+/2+}$/[Co(phen)$_3$]$^{3+/2+}$, NO$_3$$^-$/NO$_2$– etc [18]. However, this type of Z-scheme photocatalytic system suffers from a variety of drawbacks including the unavoidable backward reactions between electron mediators and semiconductors, their lack of long-term stability due to the loss of the A/D pairs, the reduced light absorption of the semiconductors induced by the shielding effect of the A/D pairs as well as the restriction of their applications only in the liquid phase reaction, etc. To overcome these shortcomings of the A/D pairs containing Z-scheme photocatalytic systems, all-solid-state Z-scheme photocatalytic systems which employ
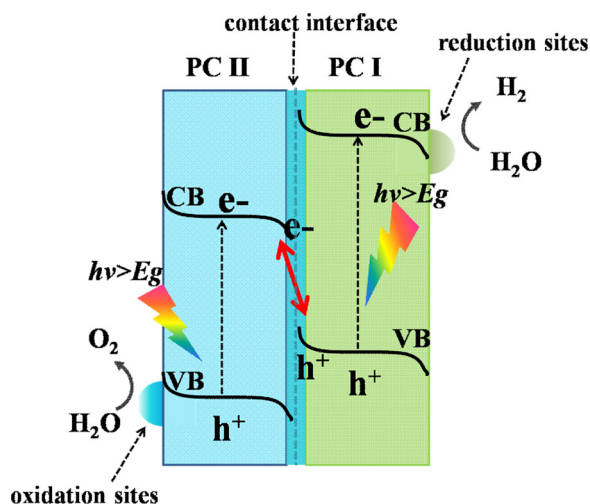
---

* Corresponding authors.
  E-mail addresses: xietf@jlu.edu.cn (T. Xie), zhaohuili1969@yahoo.com (Z. Li).

Scheme 1. An illustration of a direct Z-scheme photocatalytic system.

a solid conductor as the electron mediator have been developed [19,20]. The incorporation of the solid conductor as an electron mediator creates Ohmic contact with low contact resistance between the semiconductor/conductor interfaces, which makes the photogenerated electrons transfer from PC II through the Ohmic contact to combine with the photogenerated holes of PC I facilely. Those with excellent conductivity, including noble metal nanoparticles like Au [21], Ag [22], some metal oxide like ITO [23], as well as RGO [20,24], have all been used to construct this kind of all-solid-state Z-scheme photocatalytic systems, which have been used in photocatalytic degradation of pollutants, CO_2 reduction and organic syntheses [25].

Since the quasi-continuous solid-solid contact interface between two semiconductor-based photocatalysts can also form the Ohmic contact, all-solid-state Z-scheme photocatalytic systems constructed just from two semiconductors without the presence of the conductor have also been reported recently [26,27]. In such a photocatalytic system, Ohmic contact forms between the interfaces of two semiconductors and the solid-solid interfaces serve as the recombination center for the photogenerated charge carriers. Even though the charge transfer in these two component systems may not be as efficient as that in the conductor containing ternary Z-scheme systems, the two-component Z-scheme systems share many similarities with the three component ones. In addition, the electrical resistance of the solid-solid contact interface in these two component Z-scheme systems can still be tuned by optimizing the formation of the two semiconductor systems [21,28–31]. However, although the development of two-component Z-scheme photocatalytic systems have been extensively studied, only a few ones have been reported for overall water splitting [20,28,32,33] under visible light since as compared with other photocatalytic applications, overall water splitting is extremely challenging due to the simultaneous water reduction and oxidation to produce H_2 and O_2, let alone to say, the formation of the O–O bond involves a very complex multi-electron transfer process [34–36].

Surely, the fabrication of an efficient two-component Z-scheme photocatalytic system for visible light induced overall water splitting should meet those required for the construction of common two component Z-scheme photocatalytic systems, ie, both semiconductors should be responsive in the visible light region, with the bottom of the CB of PC I locates at potential negative enough for H_2 evolution, while the top of VB of PC II locates at potential positive enough for O_2 evolution. In addition, the contact interface between PC I and PC II should be well optimized for a facile transfer of the photogenerated electrons from PC II to combine with the photogenerated holes of PC I as shown in Scheme 1. This can be realized by tuning the geometry and morphology of both semiconductors and their interactions via different

synthetic strategies. Last but not the least, both co-catalysts for H_2 and O_2 evolution should be selectively deposited on PC I and PC II respectively. Therefore a rational selection of two semiconductors and delicate synthesis to optimize the interface is important to obtain an efficient two-component Z-scheme photocatalytic system for overall water splitting under visible light region, which is still very challenging.

Herein, hexagonal $ZnIn_2S_4$ and WO_3 were chosen respectively as PC I and PC II to construct a two-component Z-scheme photocatalytic system for overall water splitting under visible light. Hexagonal $ZnIn_2S_4$, a ternary chalcogenide with a bandgap of ca. 2.16 eV and the bottom of its CB locates at -0.94 V vs NHE, has been shown to be an effective visible light driven photocatalyst for water reduction to produce H_2 [37–40]. Hexagonal WO_3, with a band gap of ca. 2.60 eV [41] and the top of the VB locates at 2.66 V has been demonstrated to be effective for photocatalytic water oxidation [42,43]. The band structures of hexagonal $ZnIn_2S_4$ and WO_3 suggest that they are suitable candidates for the fabrication of a Z-scheme system for photocatalytic overall water splitting under visible light. Therefore, in this manuscript we reported the self-assembly of $ZnIn_2S_4$ thin nanosheets on the surface of hexagonal WO_3 nanorods. The further selective deposition of PtS and MnO_2, the co-catalysts for H_2 and O_2 evolution respectively, on the surface of hexagonal $ZnIn_2S_4$ and WO_3 enables the resultant PtS-$ZnIn_2S_4$/WO_3-MnO_2 to behave as a Z-scheme photocatalytic system for efficient overall water splitting under visible light. The optimized AQY of PtS-$ZnIn_2S_4$/WO_3-MnO_2 for H_2 evolution was determined to be ca. 0.50% at 420 nm. As compared with a mechanical mixture of PtS deposited hexagonal $ZnIn_2S_4$ and MnO_2 deposited hexagonal WO_3, the resultant PtS-$ZnIn_2S_4$/WO_3-MnO_2 system shows much higher activity for photocatalytic overall water splitting, suggesting that a rational design and fabrication of the all-solid state Z-scheme photocatalytic system is important to realize its efficient photocatalytic water splitting under visible light.

2. Experimental

2.1. Preparations

All the reagents are analytical grade and used without further purifications. To prepare WO_3·H_2O nanoplates, Na_2WO_4·$2H_2O$ (0.330 g, 1 mmol) was dissolved in 30 mL deionized water. HCl (6 mol·L^{-1}) was added drop-wisely to the solution until the pH of the solution reached 1.5. NaCl (0.117 g, 2 mmol) and $H_2C_2O_4$ (0.0904 g, 1 mmol) were added and the resultant solution was transferred to a 50 mL Teflon liner, sealed in the stainless steel autoclave and heated at 120 °C for 12 h. After cooling to room temperature, the precipitate was collected by centrifugation, washed with deionized water and ethanol and dried at 60 °C [44].

$ZnIn_2S_4$/WO_3 nanocomposites with different molar ratio of $ZnIn_2S_4$/WO_3 (varied from 0.1 to 0.3) were obtained by self-assembly of hexagonal $ZnIn_2S_4$ from $ZnCl_2$, $InCl_3$·$4H_2O$ and TAA in the presence of preformed orthorhombic WO_3·H_2O nanoplates. To synthesize $ZnIn_2S_4$/WO_3 nanocomposites, different amount of the as-obtained WO_3·H_2O nanoplates were dispersed in a mixed solvent (30 mL) containing water and ethanol in 1:1 ratio. Then $ZnCl_2$ (0.0544 g, 0.4 mmol), $InCl_3$·$4H_2O$ (0.234 g, 0.8 mmol) and TAA (0.120 g, 1.6 mmol) were added to the above suspension under vigorous stirring. The suspension was transferred to a 50 mL Teflon-lined autoclave, sealed and heated at 180 °C for 24 h. After cooling to room temperature, the resultant product was collected by centrifugation, washed with deionized water and absolute ethanol and dried at 60 °C. $ZnIn_2S_4$/WO_3 nanocomposites with different amount of $ZnIn_2S_4$ are denoted as x%$ZnIn_2S_4$/WO_3 (x is the molar ratio of $ZnIn_2S_4$: WO_3, x = 10, 20 and 30).

The selective deposition of PtS and MnO_2 on $ZnIn_2S_4$ and WO_3 respectively were carried out via photo-reduction of H_2PtCl_6 and photo-oxidation of $MnCl_2$ simultaneously over $ZnIn_2S_4$/WO_3. Take 20% $ZnIn_2S_4$/WO_3 as an example, 150 mg of 20%$ZnIn_2S_4$/WO_3 was

suspended in an aqueous solution containing a certain amount of H_2PtCl_6 and $MnCl_2$. The resultant suspension was irradiated with a 300 W Xe lamp for 4 h. The resultant products were filtered, washed with de-ionized water and absolute ethanol and dried overnight at 60 °C in a vacuum oven. $ZnIn_2S_4/WO_3$ selectively deposited with different amount of PtS and MnO_2 respectively on $ZnIn_2S_4$ and WO_3 were denoted as x%PtS-$ZnIn_2S_4$/WO_3-y%MnO_2, where x and y refer to the mass ratio of PtS:$ZnIn_2S_4$ and MnO_2:WO_3, respectively (x = 0.25, 0.5, and 1.0, y = 1.0, 3.0 and 5.0). For comparison, 0.5%PtS-$ZnIn_2S_4$ and 3.0% MnO_2-WO_3 were also prepared. Bare $ZnIn_2S_4$ was prepared similar to that of $ZnIn_2S_4/WO_3$ in absence of performed $WO_3\cdot H_2O$ nanoplates. The deposition of PtS on $ZnIn_2S_4$ was realized by photo-reduction of H_2PtCl_6 in the presence of methanol as a sacrificial agent. The performed $WO_3\cdot H_2O$ nanoplates was treated solvothermally at 180 °C for 24 h to transform it to hexagonal WO_3 nanorods before the deposition of MnO_2, which was realized by photo-oxidation of $MnCl_2$ in the presence of $AgNO_3$ as a sacrificial agent. In addition, 0.5%PtS-20%$ZnIn_2S_4$/WO_3 and 20%$ZnIn_2S_4$/WO_3-3.0%MnO_2 were also prepared via similar procedures.

2.2. Characterizations

The X-ray diffraction (XRD) patterns of the products were carried out on a D8 Advance X-ray diffractometer (Bruker, Germany) using Cu K_α ($\lambda = 1.5406$ Å) radiation at a voltage of 40 kV and 40 mA. XRD patterns were scanned over the angular range of 10-80° (2θ) with a step size of 0.02°. The transmission electron microscopy (TEM) and high resolution transmission electron microscopy (HRTEM) images were obtained in a JEOL model JEM 2010 EX instrument at an accelerating voltage of 200 kV. The SEM image was obtained on a field emission scanning electron microscopy (SEM) (JSM-6700 F). The powder particles were supported on a carbon film coated on a 3 mm diameter fine-mesh copper grid. Zeta-potential (ξ) measurements of the samples were determined by dynamic light scattering analysis (Zeta sizer 3000HSA) at a room temperature of 25 °C. X-ray photoelectron spectroscopy (XPS) measurements were performed on a PHI Quantum 2000 XPS system (PHI, USA) with a monochromatic Al K_α source and a charge neutralizer. All of the binding energies were referred to the C 1s peak at 284.6 eV of the surface adventitious carbon. UV–vis diffraction spectra (UV–vis DRS) of the powders were obtained for the dry pressed disk samples using a UV–vis spectrophotometer (Cary 7000 Scan Spectrophotometers, Varian). $BaSO_4$ was used as a reflectance standard. The work function measurement was carried out on a Kelvin probe instrument (SKP 5050, KP Technology Ltd, Scotland, UK). Electrochemical impedance spectroscopy (EIS) and transient photocurrent responses were measured on an electrochemical analyzer (Zahner, Germany) in a standard three-electrode system using the as-obtained sample as the working electrode (with an active area of ~0.25 cm^2), a Pt wire as the counter electrode, and Ag/AgCl (saturated KCl) as a reference electrode. Impedance data were fitted with Z SimpWin software (Princeton Applied Research). The surface photovoltage (SPV) measurement system consisted of a source of monochromatic light, a lock-in amplifier (SR830- DSP) with a light chopper (SR540), a photovoltaic cell, and a computer. A 500 W xenon lamp (CHFXQ500 W, Global Xenon Lamp Power) and a double-prism monochromator (Hilger and Watts, D 300) provided monochromatic light. The samples were studied without further treatment during the SPV measurements, and the contact between samples and the indium tin oxide (ITO) electrode was not ohmic when we carried out the measurement of surface photovoltage. The construction of the photovoltaic cell is a sandwich-like structure of ITO–sample–ITO.

2.3. Photocatalytic water splitting

Photocatalytic water splitting was carried out in a closed gas circulation and evacuation system fitted with a top Pyrex window (LABSOLAR-H_2 II, Beijing Perfect Light Technology Co. Ltd.). 50 mg of photocatalyst was dispersed in 100 mL of pure water. The reaction system was irradiated with a 300 W Xe lamp equipped with both 420 nm and 800 nm cutoff filters to provide the visible light irradiation. The temperature of the reaction system was maintained at room temperature by a flow of cooling water during the photocatalytic reaction. The amount of H_2 and O_2 evolved were determined with an on-line gas chromatography equipped with a MS-5A column and a TCD detector. The AQYs for photocatalytic H_2 production from water splitting were represented as AQY% = (2 × number of hydrogen molecules formed) / (number of incident photons) × 100%

3. Results and discussion

$ZnIn_2S_4/WO_3$ was prepared via a two-step procedure by self-assembly of hexagonal $ZnIn_2S_4$ in the presence of preformed $WO_3\cdot H_2O$ nanoplates. Orthorhombic $WO_3\cdot H_2O$ nanoplates were first obtained via a hydrothermally treatment of Na_2WO_4 in the presence of HCl (Supporting Fig. S1 and Fig. S2). A further solvothermal treatment of In^{3+}, Zn^{2+} and TAA in the presence of preformed orthorhombic $WO_3\cdot H_2O$ nanoplates at 180 °C for 24 h led to the formation of $ZnIn_2S_4$/WO_3 nanocomposites. The XRD of the as-obtained product shows 2θ peaks at values of 21.6°, 27.7° and 47.2°, in agreement with (006), (102) and (110) crystallographic planes of hexagonal $ZnIn_2S_4$ (JCPDS#072-0773), as well as 14.0°, 22.7°, 24.3°, 28.2°, 33.6°, 36.6°, 49.9°, 55.3°, 58.1° and 63.5° assignable to (100), (001), (110), (200), (111), (201), (220), (202), (400) and (401) crystallographic planes of hexagonal WO_3 (JCPDS#033-1387) (Fig. 1). This indicates that accompanied by the self-assembly of hexagonal $ZnIn_2S_4$, orthorhombic $WO_3\cdot H_2O$ has been transformed to hexagonal WO_3 during the solvothermal treatment. The TEM image of 20%$ZnIn_2S_4$/WO_3 shows that thin $ZnIn_2S_4$ nanosheets with lateral size of ca. 35 × 15 nm are deposited on the surface of WO_3 nanorods, with a diameter of about 60 nm (Supporting Fig. S3)

To study the formation of $ZnIn_2S_4/WO_3$ nanostructures, the products obtained by reacting the precursors of $ZnIn_2S_4$ and preformed orthorhombic $WO_3\cdot H_2O$ nanoplates solvothermally for different time were isolated and characterized. The XRD of the product obtained after reacting for 1 h shows that, in addition to those belong to orthorhombic $WO_3\cdot H_2O$, 2θ peaks at values of 14.0°, 28.2° and 36. 6°, assignable to (100), (200) and (201) crystallographic planes of hexagonal WO_3 indicating the partial transformation of orthorhombic $WO_3\cdot H_2O$ to hexagonal WO_3 (Supporting Fig. S4(a)). The TEM image of the product obtained at this time shows a complex structure composed of both $WO_3\cdot H_2O$ nanoplates and scattered small WO_3 nanorods (Supporting
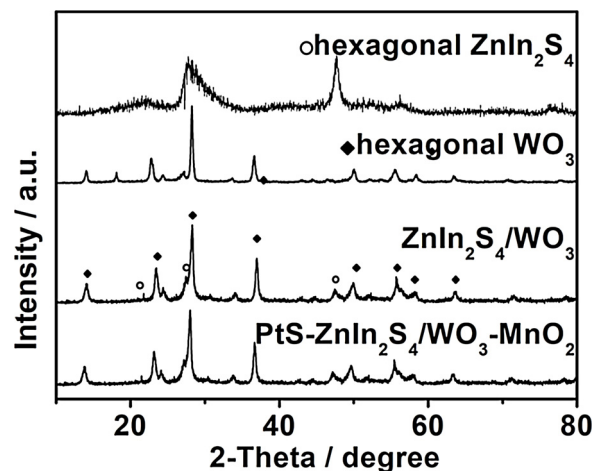

Fig. 1. XRD patterns of the as-obtained hexagonal $ZnIn_2S_4$, WO_3, $ZnIn_2S_4$/WO_3 and PtS-$ZnIn_2S_4$/WO_3-MnO_2.
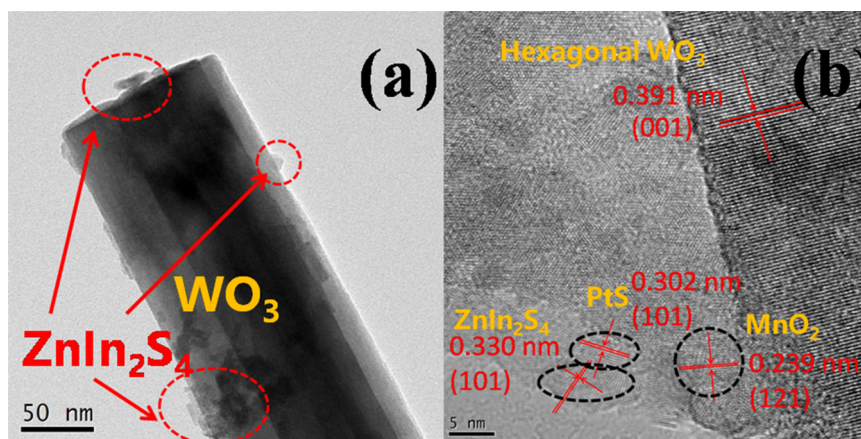
Fig. 2. (a) TEM image and (b) HRTEM image of 0.5%PtS-20%ZnIn$_2$S$_4$/WO$_3$-3.0%MnO$_2$ nanocomposite.

Fig. S5(a)). Lattice fringes of 0.536 nm corresponding to (020) crystallographic plane of orthorhombic WO$_3$·H$_2$O as well as 0.391 nm for (001) crystallographic plane of hexagonal WO$_3$ are observed in the HRTEM image, suggesting the coexistence of both orthorhombic and hexagonal WO$_3$ (Supporting Fig. S5(b)). When the reaction time was prolonged to 3 h, the XRD of the isolated product shows 2θ peaks at values of 27.7° and 47.2°, assignable to hexagonal ZnIn$_2$S$_4$, suggesting the formation of hexagonal ZnIn$_2$S$_4$, in addition to the diffraction peaks ascribed to both orthorhombic WO$_3$·H$_2$O and hexagonal WO$_3$ (Supporting Fig. S4(b)). The TEM image of the product obtained at this time shows that thin nanosheets are coated on the surface of the WO$_3$ nanorods (Supporting Fig. S5(c)). In addition to the lattice fringes belong to two polymorphs of WO$_3$, clear lattice fringes of 0.330 nm assigned to (101) crystallographic plane of hexagonal ZnIn$_2$S$_4$ was also observed (Supporting Fig. S5(d)). When the reaction was stopped at 6 h, in addition to those belong to hexagonal ZnIn$_2$S$_4$, the XRD of the isolated product shows only the diffraction peaks corresponding to hexagonal WO$_3$, indicating that orthorhombic WO$_3$·H$_2$O has been completely transformed to hexagonal WO$_3$ by this time (Supporting Fig. S4(c)). The TEM image confirms that the original WO$_3$·H$_2$O nanoplates have been transformed to nanorods of ca. 60 nm in diameter, with ZnIn$_2$S$_4$ thin nanosheets coated on its surface (Supporting Fig. S5(e)). Accordingly, the HRTEM image shows only lattice fringes assignable to hexagonal ZnIn$_2$S$_4$ and WO$_3$ (Supporting Fig. S5(f)). Although the XRD pattern of the product isolated after 24 h shows similar diffractions peaks as that obtained after reacting for 6 h, the intensity of the 2θ peaks at values of 28.2° and 47.2° increase, indicating the improved crystallinity of the obtained hexagonal WO$_3$ and ZnIn$_2$S$_4$.

Based on the above observations, the formation of ZnIn$_2$S$_4$/WO$_3$ nanocomposite is illustrated (Supporting Fig. S6). Since orthorhombic WO$_3$·H$_2$O nanoplates possess strong negatively charged surface with zeta potential value of -27.3 mV in pure water, positive metal ions Zn^{2+} and In^{3+} can absorb on the surface of orthorhombic WO$_3$·H$_2$O nanoplates. The solvothermal treatment of WO$_3$·H$_2$O nanoplates in ethanol at 180 °C weaken the interaction between H$_2$O molecule and WO$_3$, resulting in the dehydration of WO$_3$·H$_2$O. The loss of structural H$_2$O in WO$_3$·H$_2$O nanoplates provides space for WO$_6$ octrahedra in orthorhombic structure to shift in the layers perpendicular to the c-axis by $a/2$. Since orthorhombic WO$_3$·H$_2$O shares similar atomic arrangement in (0001) plane as that in hexagonal WO$_3$ except that a translation of a/2 of half of the layers perpendicular to c is required, the distortion and shift of the WO$_6$ octahedra results in the phase transition from orthorhombic to hexagonal phase. Such a phase transformation mechanism was reported previously [45]. In addition, as previously observed on the formation of hexagonal ZnO nanorods, the growth rate along the polar direction (c-axes) in the hexagonal WO$_3$ is slow, which results in the formation of 1D nanorod structures [46]. In the meantime,

TAA was decomposed to release S^{2-} ions upon heated, which can react with the surface adsorbed Zn^{2+} and In^{3+} ions to form hexagonal ZnIn$_2$S$_4$ nucleus on the surface of WO$_3$. The further growth of ZnIn$_2$S$_4$ nucleus led to the formation of small thin nanosheets on the surface of WO$_3$ nanorods.

To make ZnIn$_2$S$_4$/WO$_3$ nanocomposites work for photocatalytic overall water splitting, PtS and MnO$_2$, co-catalysts for H$_2$ and O$_2$ evolution, should be selectively deposited on ZnIn$_2$S$_4$ and WO$_3$, respectively. The XRD patterns have no obvious change after the deposition of PtS or/and MnO$_2$ on ZnIn$_2$S$_4$/WO$_3$ (Supporting Fig. S7 and Fig. 1). The selective deposition of PtS on ZnIn$_2$S$_4$ and MnO$_2$ on WO$_3$ were realized via a simultaneous photo-reduction of H$_2$PtCl$_6$ and photo-oxidation of MnCl$_2$ over ZnIn$_2$S$_4$/WO$_3$ nanocomposites under visible light. Since the CB of hexagonal ZnIn$_2$S$_4$ locates at –0.94 V vs NHE, which is more negative than E(PtCl$_6^{2-}$/Pt^{2+}) (0.21 V vs NHE), the photogenerated electrons in ZnIn$_2$S$_4$ can reduce PtCl$_6^{2-}$ to form surface adsorbed Pt^{2+}, which can further react with S^{2-} to form PtS. The photo-reduction of PtCl$_6^{2-}$ over ZnIn$_2$S$_4$ to form surface deposited PtS for photocatalytic H$_2$ evolution has been reported previously [47]. Due to a less negative CB of hexagonal WO$_3$ (0.06 V vs NHE) as compared with E(PtCl$_6^{2-}$/Pt^{2+}), the photoreduction of PtCl$_6^{2-}$ is unlikely to occur on the surface of hexagonal WO$_3$. In the meantime, the VB position of hexagonal WO$_3$ located at 2.66 V vs NHE, which is more positive than E(MnO$_2$/Mn^{2+}) (1.23 V vs NHE). It is therefore thermodynamically favorable for the photo-oxidation of MnCl$_2$ to form MnO$_2$ on the surface of hexagonal WO$_3$. Similarly, due to a less positive position of the VB of hexagonal ZnIn$_2$S$_4$, the photo-oxidation of Mn^{2+} to form MnO$_2$ is unlikely to occur on the surface of hexagonal ZnIn$_2$S$_4$. The synchronous consumptions of the photogenerated electrons in hexagonal ZnIn$_2$S$_4$ and the photogenerated holes in hexagonal WO$_3$ leave the holes in ZnIn$_2$S$_4$ and the electrons in hexagonal WO$_3$, which can recombine through the interfaces between ZnIn$_2$S$_4$ and WO$_3$ to complete the whole photocatalytic cycle.

The selective deposition of PtS on ZnIn$_2$S$_4$ and MnO$_2$ on WO$_3$ was confirmed by both the TEM and HRTEM images of the as-obtained PtS-ZnIn$_2$S$_4$/WO$_3$-MnO$_2$ nanocomposite. The TEM and SEM images of 0.5% PtS-20%ZnIn$_2$S$_4$/WO$_3$-3.0%MnO$_2$ nanocomposite shows that small ZnIn$_2$S$_4$ nanosheet with a lateral size of ca. 35 × 15 nm was deposited on the surface of WO$_3$ nanorods with a diameter of about 60 nm (Fig. 2a and Supporting Fig. S8). The HRTEM image shows that in addition to lattice fringes of 0.391 nm corresponding to (001) crystallographic plane of hexagonal WO$_3$ and 0.330 nm corresponding to (101) crystallographic plane of hexagonal ZnIn$_2$S$_4$, clear lattice fringes of 0.239 nm and 0.302 nm attributable to (121) plane of MnO$_2$ and (101) plane of PtS, respectively, can also be observed (Fig. 2b). In addition, the XPS spectra of PtS-ZnIn$_2$S$_4$/WO$_3$-MnO$_2$ confirm the existence of Pt and Mn. The XPS spectrum in the Pt 4f region shows two peaks at 75.5
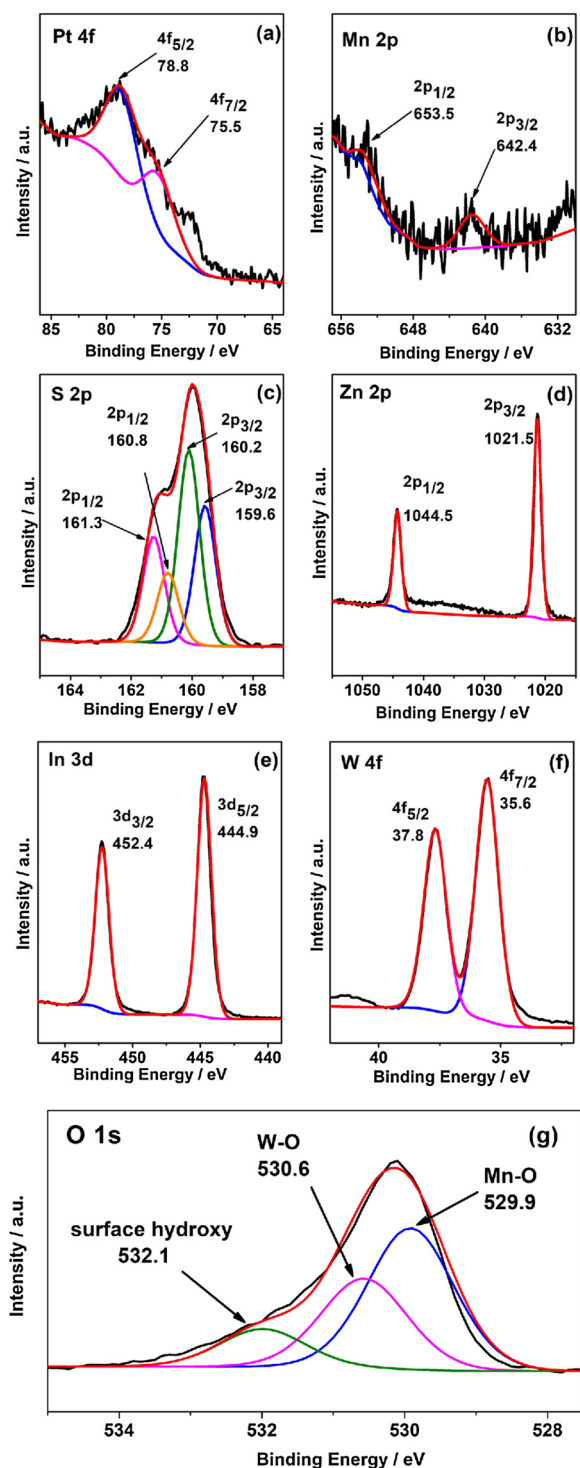
Fig. 4. UV–vis DRS spectra of (a) hexagonal $ZnIn_2S_4$; (b) hexagonal WO_3 (c) $20\%ZnIn_2S_4/WO_3$ nanocomposite; (d) $0.5\%PtS-20\%ZnIn_2S_4/WO_3-3.0\%MnO_2$.

binding energy [48], while the peaks of W^{6+} 4f (35.6 and 37.8 eV) shift towards lower binding energy [41] (Fig. 3d–f), suggesting the existence of interaction between WO_3 and $ZnIn_2S_4$ in the nanocomposites. Accordingly, the XPS in the O 1s region exhibits three peaks at 529.9, 530.6 and 532.1 eV, which are ascribed to the lattice O in MnO_2 and WO_3 as well as O in the surface hydroxyl groups (Fig. 3g). Besides XPS, the EDX of $PtS-ZnIn_2S_4/WO_3-MnO_2$ also shows the presence of elements of Pt and Mn in the nanocomposite (Supporting Fig. S9)

The band gap of hexagonal $ZnIn_2S_4$ and WO_3 were determined to be 2.16 and 2.60 eV respectively based on their UV–vis DRS spectra, with the tauc plots presented in Supporting Fig. S10. As compared with bare $ZnIn_2S_4$ and WO_3, an enhanced absorption in the region from 500 to 800 nm was observed over all $ZnIn_2S_4/WO_3$ nanocomposites. Based on previous studies on WO_3 systems, the light absorption in the region from 500 to 800 nm should be ascribed to the existence of oxygen vacancy in WO_3 [24]. Therefore, the enhanced light absorption in this region observed in all the $ZnIn_2S_4/WO_3$ nanocomposites indicates the generation of some oxygen vacancy in WO_3 in the formation of the $ZnIn_2S_4/WO_3$ nanocomposites (Fig. 4).

The photocatalytic overall water splitting to simultaneously produce H_2 and O_2 was investigated over the as-obtained $PtS-ZnIn_2S_4/WO_3-MnO_2$ nanocomposites under visible light. The reaction was initially carried out over $1.0\%PtS-10\%ZnIn_2S_4/WO_3-1.0\%MnO_2$ nanocomposite. It was found that the amount of H_2 and O_2 evolved increased with the irradiation time, with 0.67 μmol of H_2 and 0.28 μmol of O_2 obtained after 8 h irradiation (Fig. 5a). On the contrary, no H_2 and O_2 were detected in absence of either the photocatalyst or without the light irradiation, indicating that the simultaneous generation of H_2 and O_2 are really due to the photocatalytic water splitting over $1.0\%PtS-10\%ZnIn_2S_4/WO_3-1.0\%MnO_2$. The deviation of the ratio of evolved H_2/O_2 (0.67/0.28) from 2:1 may be due to a higher solubility of O_2 in water than H_2, an observation previously reported by Lu et al. [49]. No detectable H_2 and O_2 was detected over 10% $ZnIn_2S_4/WO_3$ without deposition of the **co**-catalysts under otherwise similar conditions, suggesting the important role of PtS and MnO_2 for the photoctalytic water splitting over $ZnIn_2S_4/WO_3$.

The ratio of $ZnIn_2S_4/WO_3$ in the nanocomposite influences the performance of nanocomposites for photocatalytic water splitting (Fig. 5b). When the amount of $ZnIn_2S_4$ in the nanocomposite raised from 10 mol% to 20 mol%, the amount of evolved H_2 and O_2 increased, with 1.88 μmol of H_2 and 0.68 μmol of O_2 evolved over $1.0\%PtS-20\%ZnIn_2S_4/WO_3-1.0\%MnO_2$ under otherwise similar condition, 2.8 times of H_2 and 2.4 times of O_2 respectively as those over $1.0\%PtS-10\%ZnIn_2S_4/WO_3-1.0\%MnO_2$. However, a further increase of the amount of $ZnIn_2S_4$ to 30 mol% resulted in a lowering of the photocatalytic

Fig. 3. XPS spectra of $PtS-ZnIn_2S_4/WO_3-MnO_2$ in (a) Pt 4f region; (b) Mn 2p region; (c) S 2p region ; (d) Zn 2p region; (e) In 3d region; (f) W 4f region; (g) O 1s region.

and 78.8 eV, indicating that Pt exists in the form of Pt^{2+} (Fig. 3a), while that in the Mn 2p region shows two peaks at 642.4 and 653.5 eV, assignable to Mn $2p_{3/2}$ and Mn $2p_{1/2}$ in MnO_2 (Fig. 3b). Accordingly, the XPS spectra in S 2p region can be deconvoluted into two sets of peaks, in which the peaks at 160.2 and 161.3 eV can be assigned to S $2p_{3/2}$ and S $2p_{1/2}$ in PtS, while the other two peaks at 159.6 and 160.80 eV can be assigned to S $2p_{3/2}$ and S $2p_{1/2}$ in $ZnIn_2S_4$ (Fig. 3c). As compared with bare $ZnIn_2S_4$ and WO_3, the peaks in both Zn 2p region (1021.5 and 1044.5 eV) and In 3d region (444.8 and 452.4 eV) shift towards higher
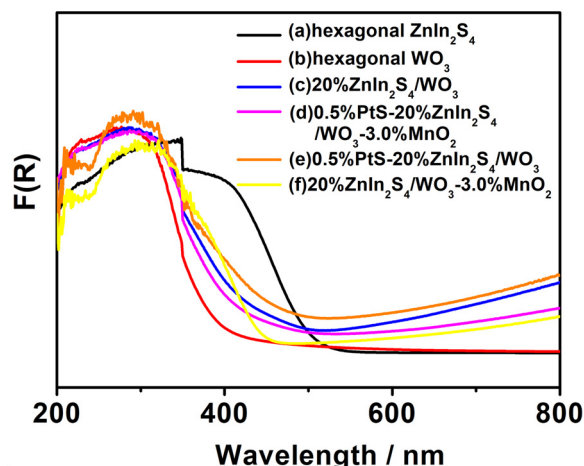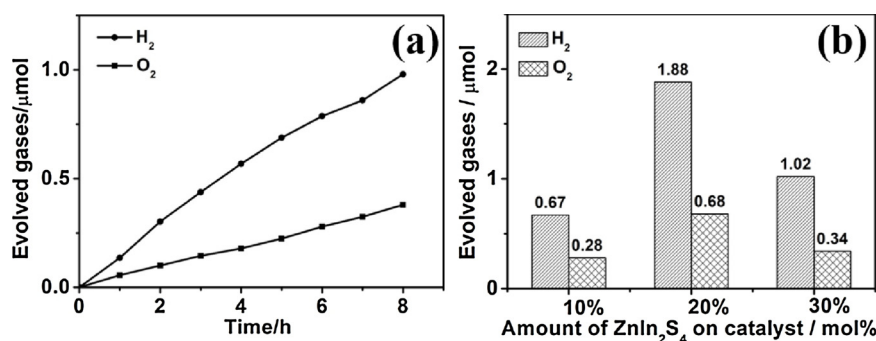
Fig. 5. (a) Time-dependent photocatalytic water splitting over $1.0\%PtS-10\%ZnIn_2S_4/WO_3-1.0\%MnO_2$; (b) Amount of H_2 and O_2 evolved in 8 h over (1)$1.0\%PtS-10\%ZnIn_2S_4/WO_3-1.0\%MnO_2$; (2)$1.0\%PtS-20\%ZnIn_2S_4/WO_3-1.0\%MnO_2$; (3) $1.0\%PtS-30\%ZnIn_2S_4/WO_3-1.0\%MO_2$ (reaction conditions: catalyst, 0.05 g; 100 mL pure water).

activity, with only 1.02 μmol of H_2 and 0.34 μmol of O_2 produced over $1.0\%PtS-30\%ZnIn_2S_4/WO_3-1.0\%MnO_2$. The observation of an optimum $ZnIn_2S_4/WO_3$ ratio is not unexpected since the rate for the generation of H_2 over $ZnIn_2S_4$ and O_2 over WO_3 should be synchronized to enable an optimum performance for overall water splitting over $ZnIn_2S_4/WO_3$ nanocomposites.

The amount of **co**-catalysts also influences the performance of nanocomposites for photocatalytic water splitting. Since $ZnIn_2S_4/WO_3$ nanocomposite containing 20 mol% of $ZnIn_2S_4$ shows an optimum performance among the investigated nanocomposites, $20\%ZnIn_2S_4/WO_3$ was chosen for the deposition of different amount of PtS and MnO_2 and their performance for water splitting was investigated (Fig. 6a). The photocatalytic performance of $PtS-ZnIn_2S_4/WO_3-MnO_2$ with a fixed MnO_2 (1.0 wt%) increased first with the amount of PtS and then decreased, with an optimum performance achieved when the amount of PtS in the nanocomposite was 0.5 wt%. About 2.78 μmol of H_2 and 1.06 μmol of O_2 were evolved after 8 h irradiation over $0.5\%PtS-20\%ZnIn_2S_4/WO_3-1.0\%MnO_2$. When the amount of PtS in the nanocomposite was fixed at 0.5 wt%, the performance increased with the amount of MnO_2 in the nanocomposites from 1.0 to 3.0 wt%, and then decreased, with an optimum performance achieved over $0.5\%PtS-20\%ZnIn_2S_4/WO_3-3.0\%MnO_2$, in which 5.94 μmol of H_2 and 2.24 μmol of O_2 were evolved in 8 h. A further increase of the amount of photocatalyst used from 50 mg to 100 mg led to higher photocatalytic activity, with 15.50 μmol of H_2 and 6.28 μmol of O_2 evolved in 8 h (Fig. 6b). The AQY value for H_2 evolution over $0.5\%PtS-20\%ZnIn_2S_4/WO_3-3.0\%MnO_2$ under optimized condition is determined to be ca. 0.50% at 420 nm.

$0.5\%PtS-20\%ZnIn_2S_4/WO_3-3.0\%MnO_2$ nanocomposite also showed high stability during photocatalytic water splitting. No obvious loss of the activity was observed after 3 cycles over a total reaction time of 24 h (Fig. 7). In addition, the unchanged XRD pattern of the photocatalyst after the long time reaction also confirms its high stability (Supporting Fig. S11).

Photocurrent responses and electrochemical impedance spectra (EIS) were carried out over hexagonal $ZnIn_2S_4$, hexagonal WO_3, $ZnIn_2S_4/WO_3$ and $PtS-ZnIn_2S_4/WO_3-MnO_2$. $PtS-ZnIn_2S_4/WO_3-MnO_2$
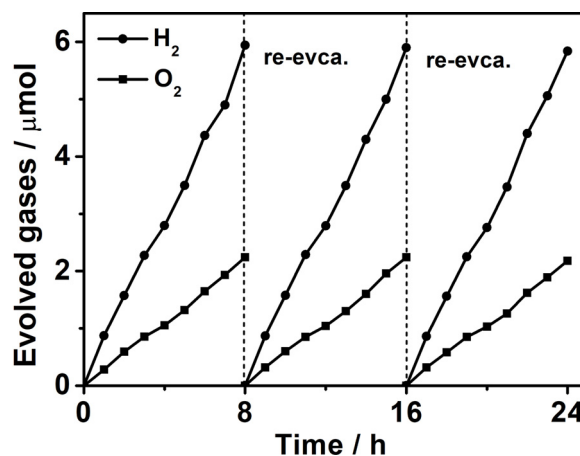

Fig. 7. Cycling of photocatalytic water splitting over $0.5\%PtS-20\%ZnIn_2S_4/WO_3-3.0\%MnO_2$ nanocomposite.

shows the highest photocurrent among the four investigated samples, followed by $ZnIn_2S_4/WO_3$ (Supporting Fig. S12a). In addition, the EIS of $PtS-ZnIn_2S_4/WO_3-MnO_2$ and $ZnIn_2S_4/WO_3$ showed the smallest and the second smallest semicircles among the four samples investigated (Supporting Fig. S12b). These results indicated that, ascribable to the matched band structure of hexagonal $ZnIn_2S_4$ and WO_3, the formation of an intimate interface between $ZnIn_2S_4$ and WO_3 is beneficial for a vectorial charge transfer in $ZnIn_2S_4/WO_3$ as compared with that in bare $ZnIn_2S_4$ and WO_3. In addition, the deposition of **co**-catalysts further facilitated the vectorial charge transfer to promote the photocatalytic water splitting over $PtS-ZnIn_2S_4/WO_3-MnO_2$.

Several controlled experiments have also been carried out to unveil the mechanism for photocatalytic water splitting over $PtS-ZnIn_2S_4/WO_3-MnO_2$. It was found that a mechanical mixture of $0.5\%PtS-ZnIn_2S_4$ and $WO_3-3.0\%MnO_2$ with a similar ratio of $ZnIn_2S_4:WO_3$ to that in $0.5\%PtS-20\%ZnIn_2S_4/WO_3-3.0\%MnO_2$ showed an inferior activity for water splitting, with only 0.86 μmol of H_2 and 0.32 μmol of O_2 evolved
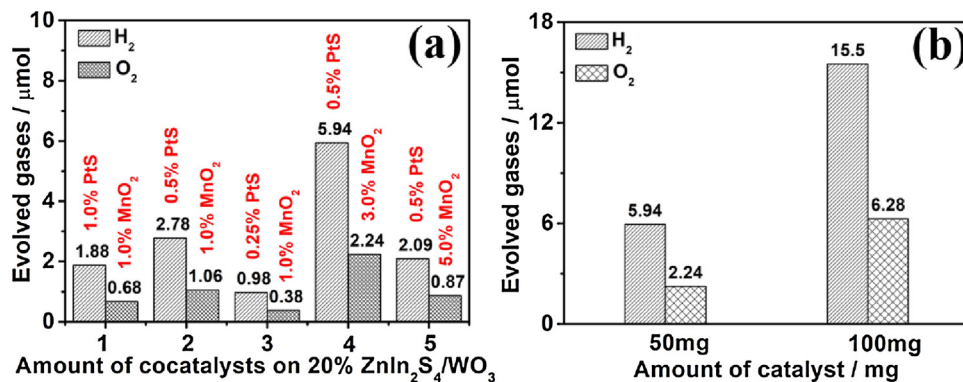

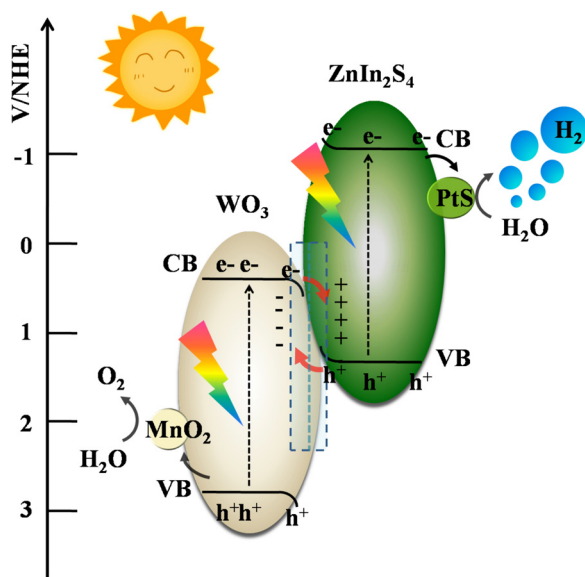**Fig. 6.** (a) Amount of H_2 and O_2 evolved in 8 h irradiation over $PtS-20\%ZnIn_2S_4/WO_3-MnO_2$ nanocomposites with (1) 1.0%PtS and 1.0%MnO_2; (2) 0.5%PtS and 1.0%MnO_2; (3) 0.25%PtS and 1.0%MnO_2; (4) 0.5%PtS and 3.0%MnO_2; (5) 0.5%PtS and 5.0%MnO_2; (b) Amount of H_2 and O_2 evolved in 8 h over different amount of $0.5\%PtS-20\%ZnIn_2S_4/WO_3-3.0\%MnO_2$ nanocomposite.

Scheme 2. Proposed mechanism for photocatalytic overall water splitting over PtS-ZnIn$_2$S$_4$/WO$_3$-MnO$_2$ nanocomposites under visible light.

in 8 h, much lower than those evolved over 0.5%PtS-20%ZnIn$_2$S$_4$/WO$_3$-3.0%MnO$_2$ under otherwise similar condition (5.94 μmol of H$_2$ and 2.24 μmol of O$_2$). In addition, neither PtS-ZnIn$_2$S$_4$ nor MnO$_2$-WO$_3$ alone showed photocatalytic activity for water splitting. Only about 1.01 μmol of H$_2$ and negligible O$_2$ were evolved after 8 h irradiation over 0.5%PtS-20%ZnIn$_2$S$_4$/WO$_3$, while 0.83 μmol of H$_2$ and 0.24 μmol of O$_2$ were produced over 20%ZnIn$_2$S$_4$/WO$_3$-3.0%MnO$_2$ under otherwise similar conditions, which were much inferior than those over 0.5% PtS-20%ZnIn$_2$S$_4$/WO$_3$-3.0%MnO$_2$. This indicates the important synergistic effect played by simultaneously deposition of PtS and MnO$_2$ on ZnIn$_2$S$_4$/WO$_3$ for photocatalytic overall water splitting (Supporting Fig. S13). These results indicate that the efficient photocatalytic water splitting over PtS-ZnIn$_2$S$_4$/WO$_3$-MnO$_2$ nanocomposites should be ascribed to an efficient coupling of photocatalytic water reduction over PtS-ZnIn$_2$S$_4$ and photocatalytic water oxidation over MnO$_2$-WO$_3$ by a Z-scheme charge pathway. Since WO$_3$ possesses a higher work function of 5.27 eV as compared with that of hexagonal ZnIn$_2$S$_4$ (4.80 eV) (Supporting Fig. S14), the formation of the interface between ZnIn$_2$S$_4$ and WO$_3$ makes the electrons transfer from ZnIn$_2$S$_4$ to WO$_3$ until an equilibrium is reached. A built-in electric field, with positively charged ZnIn$_2$S$_4$ and negatively charged WO$_3$, is thus formed. When PtS-ZnIn$_2$S$_4$/WO$_3$-MnO$_2$ is irradiated with visible light, both electrons and holes are generated on ZnIn$_2$S$_4$ and WO$_3$. The presence of the built-in electric field and the Coulomb repulsion prevent the photogenerated electrons in the CB of ZnIn$_2$S$_4$ to transfer to that of WO$_3$, even though the CB of ZnIn$_2$S$_4$ locates at a more negative position (-0.94 V vs NHE) as compared with that of WO$_3$ (0.06 V vs NHE) (Supporting Fig. S15). Similarly, the transfer of the photogenerated holes from the holes in the VB of WO$_3$ to that of ZnIn$_2$S$_4$ is also inhibited. On the contrary, the self-assembly of hexagonal ZnIn$_2$S$_4$ on the surface of WO$_3$ nanorods creates Ohmic contact in the interface between ZnIn$_2$S$_4$ and WO$_3$, which makes the photogenerated holes in the VB of ZnIn$_2$S$_4$ to recombine with the photogenerated electrons in the CB of WO$_3$ through the Ohmic contact facilely, ie, an efficient Z-scheme charge transfer pathway can be achieved. Therefore, the electrons in the CB of ZnIn$_2$S$_4$ and the holes in the VB of WO$_3$ are left and spatially separated. As a result, the photocatalytic water reduction can be realized over PtS deposited ZnIn$_2$S$_4$, while the water oxidation can be realized over MnO$_2$ deposited WO$_3$ to achieve overall water splitting (Scheme 2). The efficiency of the Z-scheme charge transfer pathway depends strongly on the interface between the two semiconductors since as evidenced from the above

controlled experiments, a mechanical mixture of PtS/ZnIn$_2$S$_4$ and MnO$_2$/WO$_3$ which lacks the required interface between ZnIn$_2$S$_4$ and WO$_3$ shows almost negligible activity for overall water splitting.

The above proposed mechanism was also supported by the CV as well as the SPV. The CV of PtS-ZnIn$_2$S$_4$/WO$_3$- MnO$_2$ shows a reduction peak occurs at -0.73 V vs NHE at pH of 6 and an oxidation peak occurs at 1.01 V vs NHE at pH of 6 (Supporting Fig. S16). The reduction potential of ZnIn$_2$S$_4$/WO$_3$ is more negative than the reduction potential of H$^+$ to H$_2$ (-0.35 V vs NHE at pH of 6), while its oxidation potential is more positive than the oxidation potential of H$_2$O to O$_2$ (0.88 V vs NHE at pH of 6), indicating that water splitting over PtS-ZnIn$_2$S$_4$/WO$_3$-MnO$_2$ is thermodynamically favorable. In addition, The SPV of bare WO$_3$ and ZnIn$_2$S$_4$ show response in the region of 300–550 nm and 300–530 nm, respectively, assignable to their band gap transition. As compared with bare WO$_3$ and ZnIn$_2$S$_4$, the photoelectric signal of ZnIn$_2$S$_4$/WO$_3$ significantly decreases (Supporting Fig. S17). A similar decrease of the photoelectric signal of CdS was also observed when it forms a Z-Scheme CdS/WO$_3$ and proposed to be attributed to the recombination of the photogenerated electrons in WO$_3$ and the photogenerated holes in CdS [50]. Therefore, the decrease of the SPV signal over current ZnIn$_2$S$_4$/WO$_3$ as compared with that of bare ZnIn$_2$S$_4$ may also suggest the existence of the Z-Scheme charge transfer pathway in ZnIn$_2$S$_4$/WO$_3$, ie, the recombination of the photogenerated electrons in WO$_3$ with the photogenerated holes in ZnIn$_2$S$_4$.

4. Conclusion

In summary, ZnIn$_2$S$_4$/WO$_3$ nanocomposites fabricated by self-assembly of hexagonal ZnIn$_2$S$_4$ in the presence of WO$_3$ were selectively deposited with PtS, the co-catalyst for H$_2$ evolution, and MnO$_2$, the co-catalyst for O$_2$ evolution. The resultant PtS-ZnIn$_2$S$_4$/WO$_3$-MnO$_2$ nanocomposites act as efficient Z-Scheme photocatalytic systems for overall water splitting under visible light. An optimum AQY for H$_2$ evolution was determined to be ca. 0.50% at 420 nm. This study demonstrates that efficient photocatalysts for overall water splitting to generate H$_2$ and O$_2$ simultaneously can be realized over Z-scheme photocatalytic systems by a rational selection of two semiconductor-based photocatalysts and optimizing its fabrication. This study also provides some guidance for the development of Z-scheme photocatalytic systems for overall water splitting under visible light.

Declaration of Competing Interest

The authors declared that they have no conflicts of interest to this work.

Appendix A. Supplementary data

Supplementary material related to this article can be found, in the online version, at doi:https://doi.org/10.1016/j.apcatb.2019.117948.

References

[1] G. Centi, S. Perathoner, ChemSusChem 3 (2010) 195–208.
[2] T. Hisatomi, J. Kubota, K. Domen, Chem. Soc. Rev. 43 (2014) 7520–7535.
[3] Nathan S. Lewis, Science 351 (2016) 353–362.
[4] J.R. Ran, J. Zhang, J.G. Yu, M. Jaroniec, S.Z. Qiao, Chem. Soc. Rev. 43 (2014) 7787–7812.
[5] X.B. Chen, S.H. Shen, L.J. Guo, S.S. Mao, Chem. Rev. 110 (2010) 6503–6570.
[6] P. Zhang, T. Wang, J.L. Gong, Chem 4 (2018) 223–225.
[7] W. Zheng, C. Li, K. Domen, Chem. Soc. Rev. 48 (2019) 2109–2125.

[8] H.J. Li, Y. Zhou, W.G. Tu, J.H. Ye, Z.G. Zou, Adv. Funct. Mater. 25 (2015) 998–1013.
[9] D.M. Fabian, S. Hu, N. Singh, F.A. Houle, T. Hisatomi, K. Domen, F.E. Osterlohf, S. Ardo, Energy Environ. Sci. 8 (2015) 2825–2850.
[10] W. Liu, L.L. Cao, W.R. Cheng, Y.J. Cao, X.K. Liu, W. Zhang, X.L. Mou, L.L. Jin, X.S. Zheng, W. Che, Q.H. Liu, T. Yao, S.Q. Wei, Angew. Chem. Int. Ed. 56 (2017) 9312–9317.
[11] G.G. Zhang, Z.A. Lan, L.H. Lin, S. Lin, X.C. Wang, Chem. Sci. 7 (2016) 3062–3066.
[12] J.H. Yang, D.G. Wang, H.X. Han, C. Li, Accounts Chem. Res. 46 (2013) 1900–1909.
[13] P. Ritterskamp, A. Kuklya, M.A. Wüstkamp, K. Kerpen, C. Weidenthaler, M. Demuth, Angew. Chem. Int. Ed. 46 (2007) 7770–7774.
[14] A.J. Bard, M.A. Fox, Acc. Chem. Res. 28 (1995) 141–145.
[15] Q. Wang, T. Hisatomi, Q.X. Jia, H. Tokudome, M. Zhong, C.Z. Wang, Z.H. Pan, T. Takata, M. Nakabayashi, N. Shibata, Y.B. Li, T.D. Sharp, A. Kudo, T. Yamada, K. Domen, Nat. Mater. 15 (2016) 611–615.
[16] K. Maeda, ACS Catal. 3 (2013) 1486–1503.
[17] Y. Miseki, S. Fujiyoshi, T. Gunji, K. Sayama, J. Phys. Chem. C 121 (2017) 9691–9697.
[18] P. Zhou, J.G. Yu, M. Jaroniec, Adv. Mater. 26 (2014) 4920–4935.
[19] H. Tada, T. Mitsui, T. Kiyonaga, T. Akita, K. Tanaka, Nat. Mater. 5 (2006) 782–786.
[20] A. Iwase, Y.H. Ng, Y. Ishiguro, A. Kudo, R. Amal, J. Am. Chem. Soc. 133 (2011) 11054–11057.
[21] H.J. Yun, H. Lee, N.D. Kim, D.M. Lee, S. Yu, J. Yi, ACS Nano 5 (2011) 4084–4090.
[22] T. Arai, S. Sato, T. Kajino, T. Morikawa, Energy Environ. Sci. 6 (2013) 1274–1282.
[23] H. Wang, H.L. Ye, B.H. Zhang, F.Q. Zhao, B.Z. Zeng, J. Mater. Chem. A 5 (2017) 10599–10608.
[24] C.C. Jia, X. Zhang, K. Matras-Postolek, B.B. Huang, P. Yang, Carbon 139 (2018) 415–426.
[25] Q.L. Xu, L.Y. Zhang, J.G. Yu, S. Wageh, A.A. Al-Ghamdi, M. Jaroniec, Mater. Today 21 (2018) 1042–1063.
[26] Q.J. Jia, A. Iwase, A. Kudo, Chem. Sci. 5 (2014) 1513–1519.
[27] J.G. Yu, S.H. Wang, J.X. Low, W. Xiao, Phys. Chem. Chem. Phys. 15 (2013) 16883–16890.
[28] Q.C. Yuan, D. Liu, N. Zhang, W. Ye, H.X. Ju, L. Shi, R. Long, J.F. Zhu, Y.J. Xiong, Angew. Chem. Int. Ed. 56 (2017) 4206–4210.
[29] D.A. Reddy, H. Park, M. Gopannagari, E.H. Kim, S. Lee, D.P. Kumar, T.K. Kim, ChemSusChem 11 (2018) 245–253.
[30] J. Jin, J.G. Yu, D.P. Guo, C. Cui, W. Ho, Small 11 (2015) 5262–5271.
[31] C.L. Zhang, S.H. Yu, Chem. Soc. Rev. 43 (2014) 4423–4448.
[32] Q. Wang, T. Hisatomi, S.S.K. Ma, Y.B. Li, K. Domen, Chem. Mater. 26 (2014) 4144–4150.
[33] M.S. Zhu, Z.C. Sun, M. Fujitsuka, T. Majima, Angew. Chem. Int. Ed. 57 (2018) 2160–2164.
[34] X.F. Yang, H. Tang, J.S. Xu, M. Antonietti, M. Shalom, ChemSusChem 8 (2015) 1350–1358.
[35] Z.G. Yi, J.H. Ye, N. Kikugawa, T. Kako, S.X. Ouyang, H. Stuart-Williams, H. Yang, J.Y. Cao, W.J. Luo, Z.S. Li, Y. Liu, R.L. Withers, Nat. Mater. 9 (2010) 559–564.
[36] K.L. Materna, R.H. Crabtree, G.W. Brudvig, Chem. Soc. Rev. 46 (2017) 6099–6110.
[37] L. Wei, Y.J. Chen, Y.P. Lin, H.S. Wu, R.S. Yuan, Z.H. Li, Appl. Catal. B: Environ. 144 (2014) 521–527.
[38] Y.J. Chen, G.H. Tian, Z.Y. Ren, K. Pan, Y.H. Shi, J.Q. Wang, H.G. Fu, ACS Appl. Mater. Interfaces 6 (2014) 13841–13849.
[39] S.H. Shen, L. Zhao, Z.H. Zhou, L.J. Guo, J. Phys. Chem. C 112 (2008) 16148–16155.
[40] L. Ye, J.L. Fu, Z. Xu, R.S. Yuan, Z.H. Li, ACS Appl. Mater. Inter. 6 (2014) 3483–3490.
[41] X.K. Zeng, Z.Y. Wang, G. Wang, T.R. Gengenbach, D.T. McCarthy, A. Deletic, J.G. Yu, X.W. Zhang, Appl. Catal. B: Environ. 218 (2017) 163–173.
[42] R. Abe, M. Higashi, K. Domen, ChemSusChem 4 (2011) 228–237.
[43] F. Amano, D. Li, B. Ohtani, Chem. Comm. 46 (2010) 2769–2771.
[44] X.D. Ma, D.L. Jiang, P. Xiao, Y. Jin, S.C. Meng, M. Chen, Catal. Sci. Technol. 7 (2017) 3481–3491.
[45] B. Gerand, G. Nowogrocki, M. Figlarz, J. Solid State Chem. 38 (1981) 312–320.
[46] X.Y. Kong, Z.L. Wang, Nano Lett. 3 (2003) 1625–1631.
[47] L.Z. Xu, X.Y. Deng, Z.H. Li, Appl. Catal. B: Environ. 234 (2018) 50–55.
[48] W.L. Yang, L. Zhang, J.F. Xie, X.D. Zhang, Q.H. Liu, T. Yao, S.Q. Wei, Q. Zhang, Y. Xie, Angew. Chem. Int. Ed. 55 (2016) 6716–6720.
[49] B. Tian, Z. Li, W.L. Zhen, X.Q. Zhang, G.X. Lu, J. Catal. 352 (2017) 572–578.
[50] L.J. Zhang, S. Li, B.K. Liu, D.J. Wang, T.F. Xie, ACS Catal. 4 (2014) 3724–3729.